Self-sacrificing template synthesis of Fe-N-C catalyst with a sponge-like porous carbon network for highly efficient oxygen reduction

Li Jiao[1], Arman Md Tanvir Alam[2], Sooeon Hwang[3], Javier Fonseca[4], Norbert Okolie[5], Ehab Shaaban[5], Gonghu Li[5], Frédéric Jaouen[6], Ershuai Liu[7], Sanjeev Mukerjee[7], Jacob Schatz Spendelow[2], David A. Cullen[*8], Qingying Jia[*7]

[1]Department of Chemical Engineering, Northeastern University, Boston, Massachusetts, 02115, United States

[2] Material Physics and Application, Los Alamos National Laboratory, Los Alamos, 87545 USA

[3]Center for Functional Nanomaterials, Brookhaven National Laboratory, Upton, New York 11973, United States

[4]Catalan Institute of Nanoscience and Nanotechnology (ICN2), CSIC and The Barcelona Institute of Science and Technology, Campus UAB, Bellaterra, 08193, Barcelona, Spain

[5]Department of Chemistry, University of New Hampshire, Durham, New Hampshire 03857, United States

[6]ICGM, Univ. Montpellier, CNRS, ENSCM, Montpellier, France

[7]Department of Chemistry and Chemical Biology, Northeastern University, Boston, Massachusetts, 02115, United States

[8]Center for Nanophase Materials Sciences, Oak Ridge National Laboratory, Oak Ridge, Tennessee 37831, USA

ABSTRACT:

Iron-nitrogen-carbon (Fe-N-C) single-atom catalysts are promising sustainable alternatives to the costly and scarce platinum (Pt) to catalyze the oxygen reduction reactions (ORR) at the cathode of polymer electrolyte membrane fuel cells (PEMFCs). However, Fe-N-C cathodes for PEMFC are made thicker than Pt/C ones, in order to compensate for the lower intrinsic ORR activities and site densities of Fe-N-C materials. The thick electrodes are bound with mass transport issues that limit their performance at high current densities, especially in H_2/air PEMFCs. Practical Fe-N-C electrodes must combine high intrinsic ORR activity, high site density and fast mass transport. Herein, we achieved an improved combination of these properties with a Fe-N-C catalyst prepared via a two-step synthesis approach, constructing first a sponge-like porous Zn-N-C substrate, followed by transmetallating Zn by Fe via chemical vapor deposition. A cathode comprising this Fe-N-C catalyst has exhibited a maximum power density of 0.53 W cm^{-2} in H_2/air PEMFC at 80 °C, and a current density of 0.74 A cm^{-2} at 0.6 V.

INTRODUCTION

The low-temperature polymer electrolyte membrane fuel cells (PEMFCs) convert chemical energy into electrical energy with potentially zero-emission, making it a promising decarbonized technology for transportation applications and portable devices. One of the major challenges for widespread deployment of PEMFCs is to disengage from its current dependence on costly and scarce platinum (Pt).[1] It is thus appealing to develop sustainable alternatives made of inexpensive and earth-abundant materials to catalyze the oxygen reduction reaction (ORR) in PEMFCs. The state-of-the-art alternatives are catalysts with atomically dispersed nitrogen-coordinated iron sites (FeN_4) covalently integrated into porous carbon matrices (denoted as Fe-N-C).[2-4] Fe-N-C catalysts have demonstrated encouraging initial ORR activity approaching that of Pt/C in H_2/O_2 PEMFCs.[5-6] However, the ORR performance of these Fe-N-C catalysts in H_2/air PEMFCs is much lower than that of Pt-based catalysts under the same conditions, especially at

high current density regimes, likely due to low accessibility of FeN_4 sites, that is in turn either intrinsic to such materials (high microporosity, low gravimetric active site density) or to the Fe-N-C cathode thickness.[7] Beside durability issues, this power performance gap in H_2/air PEMFC has hampered the replacement of Pt-based catalysts by Fe-N-C catalysts in practical PEMFC applications.

The state-of-the-art Fe-N-C catalysts exhibit high performance at elevated potentials such as 0.9 V in H_2/O_2 PEM fuel cells (all potentials in this work are given versus a reversible hydrogen electrode). This has been achieved by utilizing high catalyst loading in the range of 4-7 mg/cm^2 to increase the number of active sites per geometric area of the electrode, so as to compensate for the relatively low turnover frequency (TOF) and low gravimetric site density of FeN_4 active sites in comparison with those of Pt-based active sites in Pt/C materials.[6, 8-9] However, such high Fe-N-C loadings result in thick electrodes (> 100 μm), and high resistance towards oxygen and water transport through the catalytic layer, especially in H_2/air PEMFCs.[10] Consequently, the power densities they delivered at the desired PEMFC operating voltage (0.6-0.7 V) are rather low, making them impractical. To alleviate these issues, Fe-N-C catalysts with various morphologies and porosities have been designed using hard silica templates or washable salt templates as well as polymerization.[11-16] The main goal of these syntheses was to create hierarchical porous structures to facilitate mass transport. However, these syntheses involved complicated template fabrication and harsh template removal procedures. Furthermore, the initial ORR activities of these Fe-N-C catalysts were often reduced in the template removal processes.[17-18] It is therefore tempting to create hierarchical porous carbon structures for Fe-N-C catalysts without a template removal process. Typical approaches to preparing Fe-N-C catalysts without using a template generally start by finely mixing carbon, nitrogen, and iron precursors followed by heat treatment. The convoluted thermal evolution of iron, nitrogen, and carbon species during pyrolysis results however in a low degree of freedom to control active site density, catalyst's morphology and pore size distribution.[2] The conditions of the thermal treatment (atmosphere, duration, temperature, etc) affect the nature and number of the formed single-atom Fe-N_4 sites, that have been widely acknowledged to be responsible for the superior ORR activity of Fe-N-C catalysts.[2, 4, 19-20] Meanwhile, the morphology,

structure and chemistry of the carbon matrix of the Fe-N-C catalysts also depend on the conditions of the thermal treatment. With such an approach, it is therefore difficult to simultaneously optimize the site density and the catalyst morphology that is needed for a proper site accessibility. It would be appealing to develop a multi-step synthetic approach that deconvolutes the step at which the active site density is defined from the step at which the catalyst's morphology is defined. In our previous study, Fe-N-C catalysts with abundant and gas-accessible FeN_4 sites were prepared by chemical vapor deposition (CVD).[21] The FeN_4 sites formed via high-temperature transmetalation between gaseous $FeCl_3$ and ZnN_4 moieties from a Zn-N-C substrate are naturally accessible to the gas phase in the resulting Fe-N-C materials. In addition, the morphology of the carbon matrix of the Zn-N-C substrate had no observable changes upon the CVD process. The CVD method thus potentially allows for achieving dense Fe-N_4 sites and enhanced mass transport by constructing Zn-N-C substrates with desired morphologies for mass transport, followed by iron CVD for FeN_4 site formation. Based on this concept, we designed a Zn-N-C substrate with a multimodal pore size distribution by growing zeolitic imidazolate frameworks-8 (ZIF-8) nanoparticles on graphitic carbon nitride (g-C_3N_4) nanosheets. The resulting hybrid material has the potential to mitigate the agglomeration of ZIF-8 nanoparticles during pyrolysis. Meanwhile, the gaseous thermal decomposition products of g-C_3N_4 promote the collapse and deformation of ZIF-8 nanoparticles to form a porous nanostructure. The introduction of g-C_3N_4 benefits exposure to a high surface area of carbon matrix for hosting FeN_4 sites and facilitating mass transport through the catalyst layer. This catalyst delivers a maximum power density of 0.53 W cm^{-2} in H_2/air PEM fuel cells at 80 °C by following US DOE operation protocol.

RESULTS AND DISCUSSION

Our design principle is to construct a highly porous Zn-N-C substrate with high gas and water permeability, which can potentially not only form a high density of FeN_4 sites later on via iron CVD but also possess excellent mass transport features. Based on this principle, ZIF-8 nanocrystals were directly grown on graphitic carbon nitride to mitigate their aggregation during thermal pyrolysis so as to create and expose more surface area of Zn-N-C substrate during CVD.

The synthesis procedure is illustrated in Figure 1a while the details are given in the experimental section. To facilitate the crystal growth of ZIF-8 nanocrystals on g-C_3N_4, the latter was first exfoliated by sonication to nanosheets. Then, highly dispersed polyhedron ZIF-8 nanocrystals were grown on the g-C_3N_4 nanosheets by short synthesis description. (Figure 1b-d). X-ray diffraction (XRD) analysis shows that the ZIF-8 structure was indeed obtained (Figure 1e). The composite ZIF-8/g-C_3N_4 precursor was then pyrolyzed at 1050 °C to produce a substrate labelled as Zn-N-C_g. The latter was then converted to an iron-based catalyst (labeled as FeNC-CVD-gCN) with the iron CVD method recently reported for the first time by us [6] . The porosity of the Zn-N-C substrate was evaluated by N_2 adsorption/desorption. Types I and IV isotherms (Figure 1f) indicate the co-existence of micropores and mesopores.[22-23] In addition, the high gas uptake at the higher relative pressure ($P/P_0 > 0.9$) suggests the presence of abundant macropores. Specifically, the micropore diameter is centered at 1.78 nm with a total micropore volume of 0.6 cm^3/g. The dominant mesopore diameter is around 4.0 nm with a total mesopore volume of 0.7 cm^3/g (Figure 1g). The total surface area of Zn-N-C_g. is 944 m^2/g, higher than that of the Zn-N-C substrate (807 m^2g^{-1}) synthesized in the absence of g-C_3N_4.[6] Thus, the introduction of g-C_3N_4 contributes to the improved porous structure of the Zn-N-Cg substrate, especially promoting the formation of meso-/macropores that are desired for mass transport during PEMFC operation.

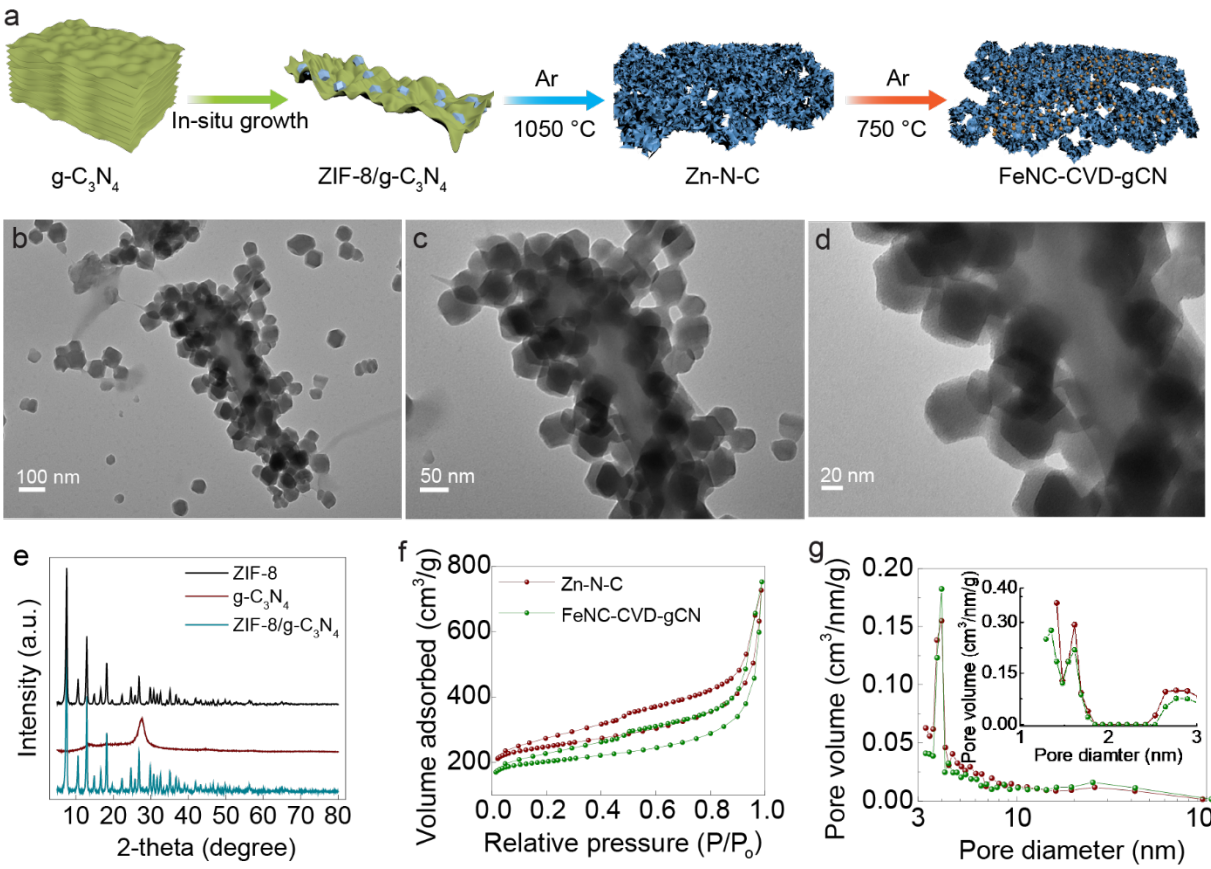

Figure 1. (a) Schematic illustration of the synthesis procedure: (1) thermal condensation of melamine, (2) exfoliation of g-C_3N_4, and growth of ZIF-8 nanoparticles on g-C_3N_4 nanosheets (labeled as ZIF-8/g-C_3N_4), (3) pyrolysis of ZIF-8/g-C_3N_4 to produce Zn-N-C substrate, (4) a CVD process to obtain Fe-N-C catalyst (labeled as FeNC-CVD-gCN). **(b)**, **(c),** and **(d)**, representative TEM images of ZIF-8/g-C_3N_4 precursor at different magnifications. (**e**) XRD patterns of the ZIF-8/g-C_3N_4 precursor, ZIF-8, and g-C_3N_4 reference. (**f**) N_2 sorption isotherm curves. (**g**) pore size distribution.

The morphology of the Zn-N-Cg substrate was further explored by high-resolution microscopy. Figure 2a and 2b show the scanning electron microscopy (SEM) images of the Zn-N-C substrate. As seen, a representative Zn-N-C particle had a three-dimensional interconnected network with abundant pores throughout. The morphology differs strikingly from the carbonaceous material derived from ZIF-8 nanocrystals in the absence of g-C_3N_4, or with the post-addition of g-C_3N_4. In those cases, the polyhedral shape of the ZIF-8 nanocrystals was crowded and preserved after pyrolysis.[21, 24] We attribute the difference to the mace-like structure of the ZIF-8/g-C_3N_4 precursor. The ZIF-8 nanoparticles and g-C_3N_4 nanosheets have a well-defined interface; the gaseous thermal decomposition products of g-C_3N_4 trigger

the collapse and deformation of ZIF-8 nanoparticles. The hypothesis is supported by the results of thermogravimetric analysis (TGA) in Fig. S1, which shows a drastic mass loss from both g-C_3N_4 and ZIF-8/g-C_3N_4 in the temperature range 500 - 800 °C. We suspect that the three-dimensional interconnected network with abundant pores benefits exposure of ZnN_4 sites for transmetalation during the CVD process than the crowded ZIF-8 nanoparticles without adding g-C_3N_4 prior to pyrolysis.

Given the essential roles of Zn and nitrogen species in the formation of FeN_4 sites, Z-contrast dark-field scanning transmission electron microscopy (STEM) images for the Zn-N-C substrate were recorded. High-intensity visible Zn sites are all over the three-dimensional frameworks of Zn-N-C particles (Figure 2c-g). The energy-dispersive X-ray spectroscopy (EDS) mapping independently indicates Zn and N sites are uniformly dispersed within the Zn-N-C substrate (Figure 2e-g). Atomic-resolution aberration-corrected annular dark-field scanning transmission electron microscope (ADF- STEM) images further demonstrate the atomic dispersion of Zn atoms in the Zn-N-C substrate (Fig. 2h-i). Each Zn atom is primarily surrounded by four nitrogen atoms (noted as ZnN_4 structure), as indicated by the fit of the Fourier Transform of the extended X-ray absorption fine structure (FT-EXAFS) spectrum at the Zn K-edge (Figure 2j). The presence of a small FT-EXAFS peak around 2 Å (without phase correction) (Figure 2j) suggests the existence of low contents of metallic zinc, in addition to the Zn-N_4 moieties.

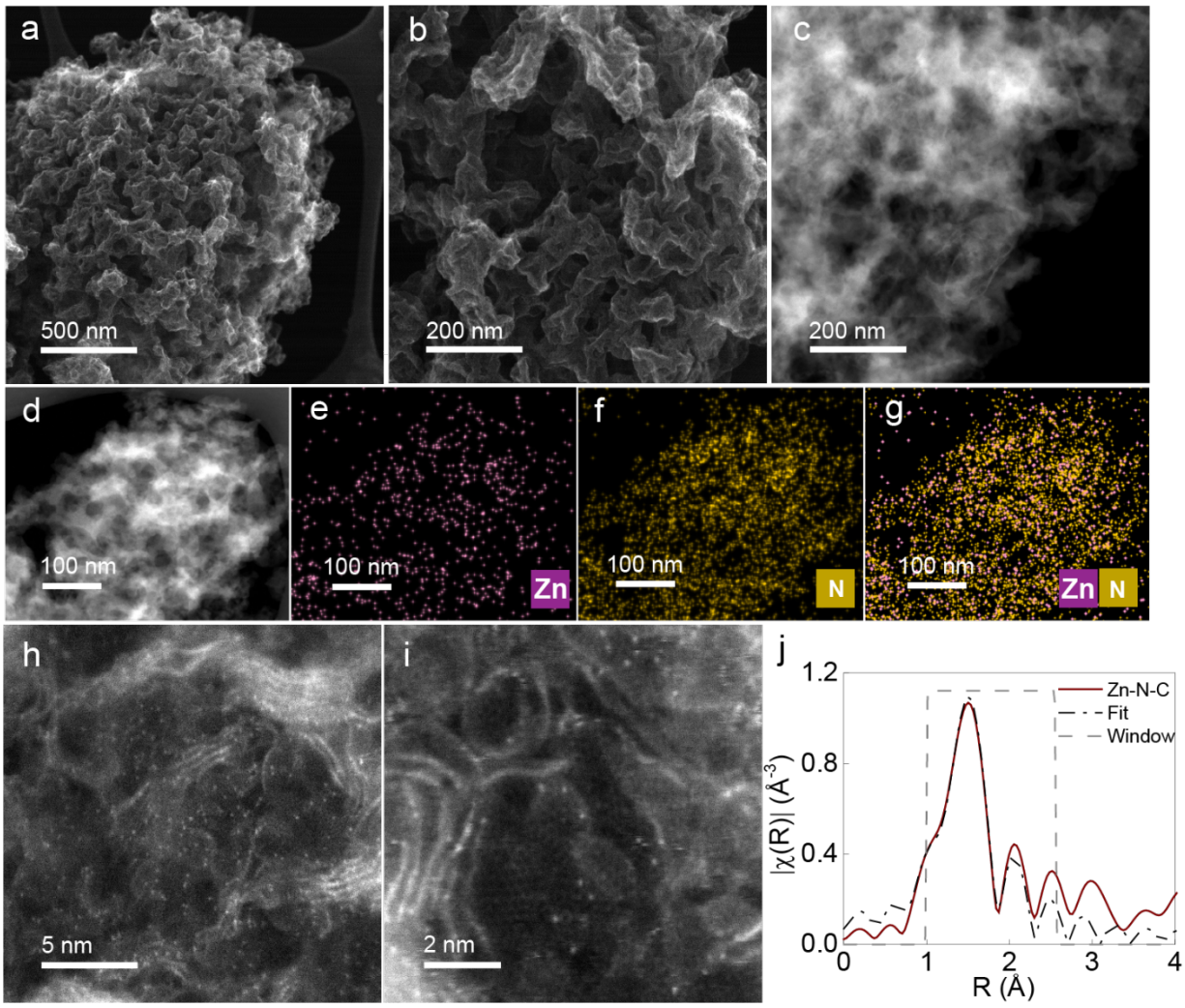

Figure 2 (**a**) and (**b**) SEM images at different magnifications. (**c**)-(**g**) Z-contrast STEM images and energy-dispersive X-ray spectroscopy (EDS) elemental distribution maps of zinc (**e**), nitrogen (**f**), and their overlapping image (**g**). (**h**) and (**i**) aberration-corrected annular dark-field (ADF) STEM images. (**j**) ex-situ Zn K-edge Fourier-transformed EXAFS spectrum and its fitting. R is interatomic distance. The indicated radial distance is not corrected for phase shift. χ(R) is the Fourier transform in the R space.

The ORR activity of FeNC-CVD-gCN catalyst was first evaluated in 0.5 M H_2SO_4 using a rotating disc electrode (RDE). A 0.85 V half-wave potential ($E_{1/2}$) was demonstrated, coupled with a well-defined diffusion-limited current density of 4.2 $mA \cdot cm^{-2}$, close to the expected value for 4 e ORR at 900 rpm (Figure 3a). Compared with Zn-N-C, the substantial increase in ORR activity highlights the essential role of iron in the superior ORR activity of the Fe-N-C catalyst in acid medium. The Tafel plot derived from the ORR polarization curve shows a kinetic current density of 16 $mA \cdot cm^{-2}$ (20 mA per milligram catalyst) at

0.8 V. This activity compares favorably with the state-of-the-art Fe-N-C catalysts.[25]

To evaluate the potential application in PEMFCs, the FeNC-CVD-gCN catalyst was integrated into the membrane electrode assembly (MEA) by blading coated on Nafion 211 membrane with Nafion D521 ionomer (Noted as MEA_blade_Nafion). The MEA_blade_Nafion was measured in a H_2/air-fed single-cell PEMFC at 50 %, 75%, and 100 % relative humidity (RH) in sequence at 80 °C. The ORR performance at 0.5 V decreases only from 955 to 864 mA/cm^2 as the humidity decreases from 100 to 75 % RH, and further decreases to 717 mA/cm^2 as the humidity decreases to 50% RH (Figure 3b). For comparison, the ORR performance of a commercial Fe-N-C (~600 m^2/g) at 0.5 V under 75% RH was only around 50% (with 35 wt% ionomer loading) or around 75% (with 45% ionomer loading) of that under 100% RH in H_2/air fed-single PEM fuel cells.[26-27] The ORR performance of Fe-N-C catalysts in high current densities is limited by the high O_2 and H^+ transport resistances due to the low hydration degree of the ionomer at lower relative humidities.[28-29] Thus, the exceptional ORR performance of the FeNC-CVD-gCN electrode at low RH suggests its excellent mass transport properties.

In order to further examine the mass transport of the FeNC-CVD-gCN cathode, the heliox (He: 79%, O_2: 21%) replaced the air in the cathode.[30-31] Such replacement generally has little effect on the lower current density, while it has less voltage loss in the higher current density. For example, at 0.5 A/cm^2, the electrode with H_2/heliox showed around 15 mV higher voltage than that with H_2/air condition. The lower voltage loss is attributed to the higher oxygen and water vapour diffusion coefficients in helium than in nitrogen.[30, 32] However, the ORR performance is almost the same in H_2/heliox and H_2/air conditions for the FeNC-CVD-gCN cathode (Figure 3b). Electrochemical impedance spectroscope (EIS) measurements were carried out at 0.5 A/cm^2 in H_2/heliox and H_2/air conditions, respectively. The impedance spectra in H_2/heliox and H_2/air conditions are nearly the same (Fig.S2). Generally, at high current density, the features at high frequencies are related to the membrane and electronic contact resistances; and the features at low frequencies are linked to catalyst layer resistance and mass transport resistance.[33-34] Thus, the FeNC-CVD-gCN cathode electrode has a similar mass transport resistance in H_2/heliox and H_2/air conditions. It further confirms the improved

mass transport of the FeNC-CVD-gCN electrode.

To explore the potential to further improve ORR performance by reducing the proton resistance across the cathode electrode , an ionomer with a lower equivalent weight (Aquivion, 720 g/mol) was used in the preparation of FeNC-CVD-gCN slurry instead of Nafion D521 (Nafion, 1100 g/mol). The comparison was made at a constant ionomer-to-carbon ratio (1.0). The slurry was blading coated on Nafion 211 membrane and further assembled into a MEA (labeled as MEA_blade_Aquivion). The MEA_blade_Aquivion was measured at the same practical H_2/air conditions as the MEA_blade_Nafion. The current density reached 85 mA/cm^2 at 0.8 V, 450 mA/cm^2 at 0.675 V and 740 mA/cm^2 at 0.6 V, much higher than that of MEA_blade_Nafion (35 mA/cm^2 at 0.8 V, 300 mA/cm^2 at 0.675 V and 582 mA/cm^2 at 0.6 V). This performance is higher than the majority of reported Fe-N-C catalysts. In specific, the performance at 0.675 V is higher than that of forty catalysts (forty-six in total) reported.[25] In addition, the maximum power density for the MEA_balde_Aquivion is 531 mW/cm^2 (Figure 3c). The MEA_blade_Aquivion shows better ORR performance by increasing proton availability across the cathode electrode. It suggests potential improvements in ORR performance for FeNC-CVD-gCN catalyst by further optimizing electrode fabrication.

The slurry of FeNC-CVD-gCN catalyst was also spraying coated on the gas diffusion layer as the cathode of the membrane electrode assembly (noted as MEA_spray_Nafion) and measured in an H_2/air-fed-single-cell system following the DOE protocol (80 °C 100 % RH, and 150 kpa). It exhibited a maximum power density of 0.475 W·cm^{-2} in hydrogen/air single-cell PEM fuel cells (Figure 3d). In addition, it reached 0.1 A·cm^2 at 0.8 V, slightly higher than that of MEA_blade_Aquivion. However, the FeNC-CVD-gCN electrode of MEA_spray_Nafion suffered from a serious water flooding issue at a high current density.

The stability of the FeNC-CVD-gCN electrode of MEA_spray_Nafion was evaluated via a voltage cycling (from 0.9 V to 0.6 V) accelerated stress test (Figure 4a). The current density at 0.8 V dropped from 0.1 A cm^{-2} to 0.045 A cm^{-2} after 1,000 voltage cycles. Along with 30,000 voltage cycles, the redox peaks gradually

diminished, while the capacitance did not change significantly (Figure 5b). Since we strongly believe the redox peaks arise from the Fe(II)/Fe(III) redox transition of the Fe-N_4 sites based on in situ X-ray absorption spectroscopy data[3, 20], the disappearance of the redox peaks suggests that the demetallation is one primary reason for the degradation. The poor stability of the Fe-N-C catalysts made by CVD observed here and previously[6] can be reasoned by CVD maximizing surface exposure of FeN_4 sites.

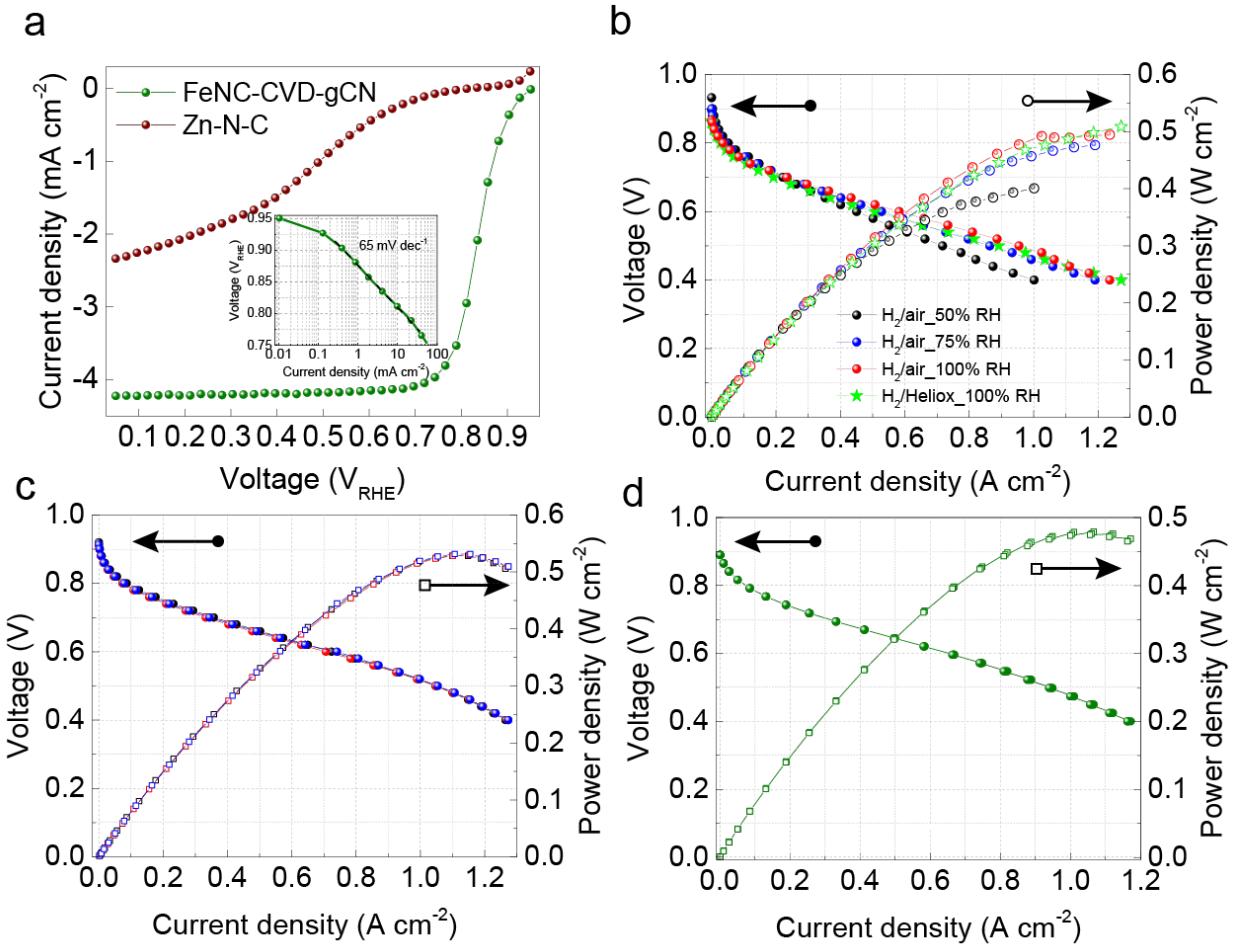

Figure 3 (**a**) steady-state rotation disc electrode (RDE) polarization curves in O_2-saturated 0.5 M H_2SO_4 at room temperature, 900 r.p.m., 20 mV potential steps from 0.05 to 0.95 V (all potentials given versus reversible hydrogen electrode (RHE)) and a 25 s potential hold at each step. 0.8 mg cm^{-2} of catalysts loading. The inset: the Tafel plot derived from the ORR polarization curve of FeNC-CVD-gCN catalyst. (**b**) Polarization and power density curves for MEA_blade_Nafion: 5.8 mg cm^{-2}, 100 % RH and 80 °C, H_2: 0.5 L/min, air or Heliox: 2.0 L/min. 150 absolute kpa. (**c**) Polarization and power density curves for MEA_blade_Aquivion: 5.8 mg cm^{-2}, 100 % RH and 80 °C, H_2: 0.5 L/min, air: 2.0 L/min, 150 absolute kpa at both anode and cathode electrodes. (**d**) Polarization and power density curves for MEA_spray_Nafion: 5.0 mg cm^{-2}, 100 % RH and 80 °C, H_2: 0.5 L/min, air: 1.0 L/min, 150 absolute kpa.

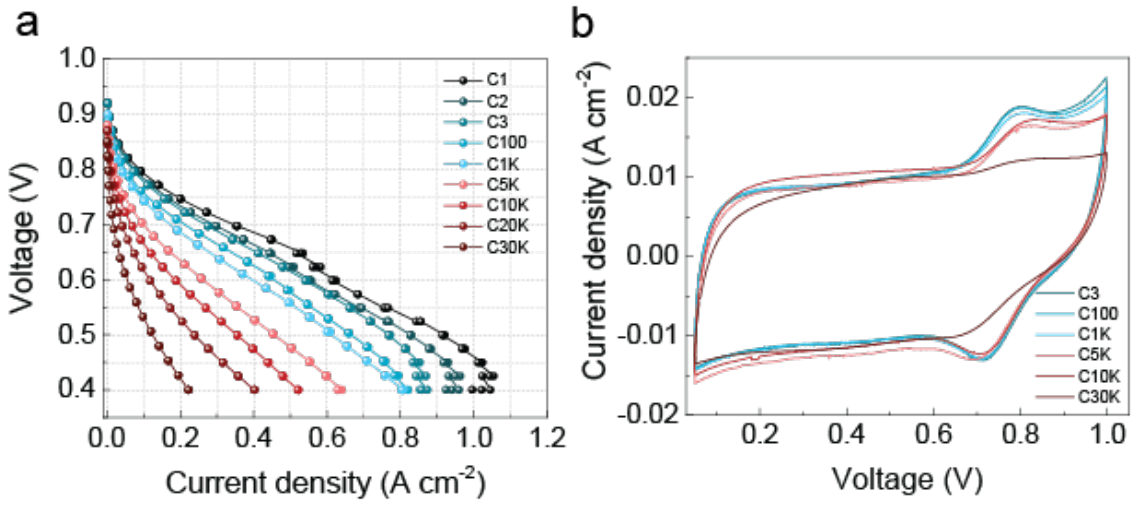

Figure 4 **(a)** The polarization curves for FeNC-CVD-gCN catalyst at initial (labeled as C1) and after different voltage cycling (labelled as C2, …C30K) from 0.9 V to 0.6 V. 5.0 mg cm^{-2}, 100 % RH and 80 °C, H_2: 0.5 L/min, air: 1.0 L/min. 150 absolute kpa at both anode and cathode electrodes, **(b)** CV curves at 20 mV/s.

To understand the source of its exceptional ORR performance, the FeNC-CVD-gCN catalyst was characterized by multiple techniques. The FeNC-CVD-gCN catalyst inherited the porous three-dimensional network features of the Zn-N-C substrate (Figure 5a-c). Specifically, the FeNC-CVD-gCN catalyst possesses a 0.5 cm^3/g micropore volume with a 1.8 nm dominant pore diameter and a 0.88 cm^3/g mesopore volume with a 4 nm dominant pore diameter (Figure 1g). The abundant mesopores and macropores are expected to increase active site utilization by improving the ionomer distribution within catalyst layers and facilitating the mass transport of gas and water within the catalyst layer. Z-contrast dark-field STEM images show iron atoms as bright dots throughout the carbon matrix without visible aggregation (Figure 5d-e). Energy-dispersive X-ray spectroscopy (EDX) mapping (Figure 5f-i) also signifies that iron and nitrogen sites were uniformly dispersed. To further identify the iron distribution, atomic-level STEM images were performed (Figure 5j). Plenty of bright dots were observed, for which the electron energy-loss spectroscopy spectrum shows the proximity of single iron and nitrogen atoms (Figure 5k). This suggests the presence of abundant FeN_x moieties in the FeNC-CVD-gCN catalyst. The Fe K-edge X-ray absorption near-edge structure (XANES) spectrum of the FeNC-CVD-gCN catalyst (Figure 5l) overlaps that of the $Fe^{III}Pc\text{-}O_2$

reference compound, which suggests that the average oxidation state of iron in the FeNC-CVD-gCN is close to +3. This precludes the presence of large amounts of metallic Fe^0 species, further supported by the absence of prominent FT-EXAFS peaks at ca 2.2 Å, characteristic for Fe-Fe interaction from metallic species (Figure 5m). The absence of FT-EXAFS signal at 2.5-2.7 angstrom also excludes the presence of significant amounts of ordered ferric oxides, and the iron therefore seems to be present as FeIIINx sites. The fitting of the FT-EXAFS spectrum with a total coordination number of the first-shell N/O scatters of ~ 5 implies the dominant iron sites are Fe-N_4-O_2, indicating that the Fe-N_4 moieties are mostly gas-accessible. These results in combination demonstrated that a porous three-dimensional network with abundant gas-accessible FeN_4 sites was achieved on the FeNC-CVD-gCN catalyst.

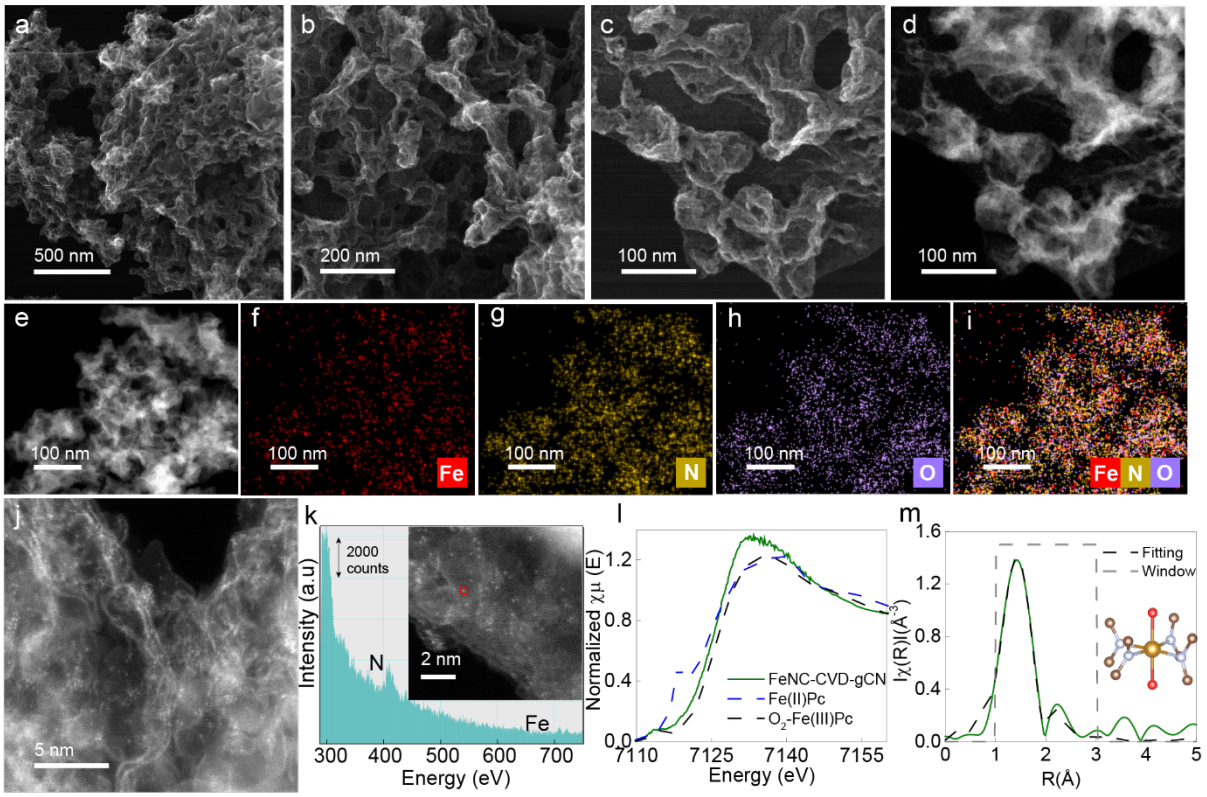

Figure 5 (**a**), (**b**) and (**c**) SEM images at different magnifications. (**d**)-(**i**) Z-contrast STEM images and EDS elemental distribution maps of iron (**f**), nitrogen (**g**), oxygen (**h**), and their overlapping image (**i**). (**j**)

aberration-corrected ADF-STEM images. (**k**) electron energy-loss spectroscopy showing the N K edge and Fe L edge acquired from a single atom (the bright dot in the inset in which an atomic-resolution AC-STEM image is displayed). (**l**) ex-situ XANES spectrum together with those of Fe (II)Pc and O_2-Fe(III)Pc reference compounds for comparison. (**m**) ex-situ Fe K-edge Fourier-transformed EXAFS spectrum and the fitting, with the O_2-Fe (III)-N_4-C_8 model presented in the inset, wherein the orange, blue, red, and brown balls represent Fe, N, O, and C atoms, respectively. R is interatomic distance. The indicated radial distance is not corrected for phase shift. χ(R) is the Fourier transform in the R space.

To understand the high activity of the FeNC-CVD-gCN catalyst, we quantified its electrochemically active site density by nitrite stripping. This measurement assumes that the nitrite anions react with FeN_x moieties to form the stable nitrosyl adduct and the adduct could be removed by performing reductive stripping in a lower potential region. The associated stripping charge allows for quantifying the number of active sites.[35-36] After exposure of FeNC-CVD-C_3N_4 electrode to NO_2^- the solution, the ORR activity was significantly decreased (Figure 6a), evidencing NO_2^- poisoning the active sites in the FeNC-CVD-gCN catalyst. Subsequently, the NO_2^- reductive stripping in the lower potential region was conducted. The associated stripping area (the grey area in Figure 6b) was integrated to calculate the stripping charge. After stripping, the ORR performance was mostly recovered (Figure 6a). Note that the number of electron transfers (three or five electrons) in nitrite stripping, which is required to calculate the charge, is currently under debate.[36-37] Assuming three electrons transfer during nitrite stripping, the site density of FeNC-CVD-gCN is around 0.8×10^{20} sites per gram of the catalyst, in the same scale of that (1.92×10^{20}) of our previous FeNC-CVD-750 catalyst but higher than the reported benchmark values.[21, 26] In good agreement with the site density quantification, the ORR activity at 0.9 V of the FeNC-CVD-gCN catalyst is lower than that of FeNC-CVD-750 catalyst. However, despite the lower site density, the maximum power density of the FeNC-CVD-gCN catalyst is higher than that of the FeNC-CVD-750 catalyst owing to the better performance at the high current density region. This result further supports the improved mass transport of the FeNC-CVD-gCN electrode.

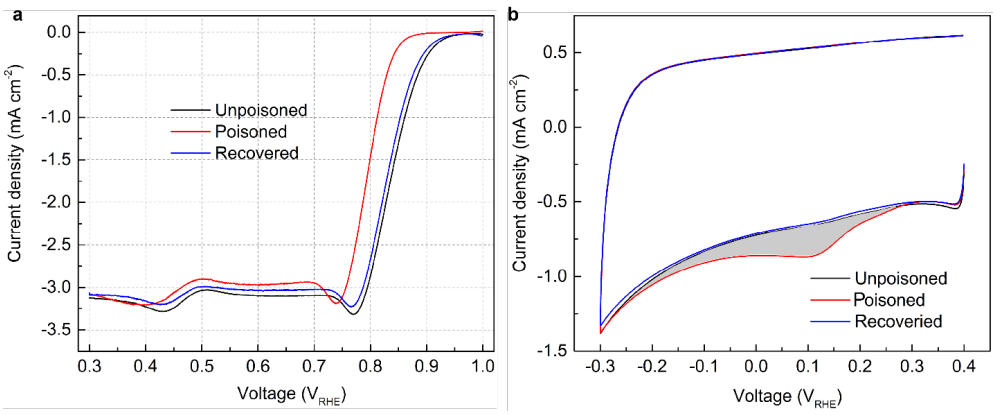

Figure 6 (a) The linear scan ORR performance without (labeled as 'Unpoisoned'), with NO_2^- poisoning (labeled as 'Poisoned') and after NO_2^- poisoning stripping (labeled as 'Recovered') in oxygen-saturated 0.5 M sodium acetate buffer (pH 5.2) with a 0.27 mg cm^{-2} loading, 10 mV/s of scan rate, and 900 r.p.m. ORR performance is corrected by the CV collected in the Ar-saturated same electrolyte with 10 mV/s of scan rate and without rotation. **(b)** NO_2^- stripping voltammetry in Ar-saturated same electrolyte with 10 mV/s of scan rate and without rotation. The grey area is associated with NO_2^- reductive stripping.

Conclusion

In this study, a Fe-N-C catalyst with a sponge-like porous network structure has been constructed with a self-sacrificing template. RDE measurements showed that the Fe-N-C catalyst exhibits high activity with a half-wave potential of 0.85 V and 16 mA cm^{-2} (20 mA per milligram catalyst) of kinetic current density at 0.8 V. The Fe-N-C cathode has demonstrated a peak power density of 0.531 W cm^{-2} in a H_2/air PEM fuel cell owing to its excellent mass transport property. It suggests that self-sacrificing template synthesis in combination with the CVD method could be implemented to optimize site densities as well as mass transport.

Experimental section

Synthesis of graphitic carbon nitride (g-C_3N_4). 6 g melamine (Sigma Aldrich) was pyrolyzed at 550 °C for 4 hours in the air in a muffle furnace. The ramping rate was 5 °C/min. The resultant yellow graphitic carbon nitride (g-C_3N_4) was ball milled for 10 minutes with a ball-to-powder mass ratio of 1 in a 35 ml grinding vial (SPEX SamplePrep, Mixer/Mill 8000M).

Synthesis of zeolitic imidazolate framework-8 /graphitic carbon nitride integrated precursor (ZIF-

8/g-C_3N_4). 0.5 g of the ball-milled g-C_3N_4 and 9.852 g of 2-methylimidazole (99%, Sigma-Aldrich) were dispersed into 500 ml methanol solution (Sigma-Aldrich) and sonicated for 10 hours. 8.924 g Zn $(NO_3)_2 \cdot 6H_2O$ (≥ 99.0%, Sigma-Aldrich) in 100 ml methanol was added to the above solution under stirring for 1 hour at room temperature. The suspension stood for 4 hours and was collected by centrifuge with fresh methanol and dried at 60 °C for 12 hours in a vacuum oven.

Synthesis of Zn-N-C substrate. 1.0 g of ZIF-8/g-C_3N_4 integrated precursor and 0.25 g of 1,10 phenanthroline (Sigma-Aldrich) were dispersed in a 50 ml solution of ethanol/water with a volume ratio of 2:1. The mixture was magnetically stirred for 2 hours and dried at 80 °C in a vacuum oven for 12 hours. The dry powders were ball milled for a half hour in a 35 ml grinding vial with a ball-to-powder mass ratio of 1-to-1. The collected powders were pyrolyzed at 1050 ℃ in argon with a ramping rate of 5 °C /min and held at 1050 ℃ for 1 hour, followed by cooling down to room temperature in argon. The powders were collected (denoted as Zn-N-C) and were stored in an 80 ℃ vacuum oven before electrochemical testing and/or physicochemical characterization to prevent adsorbing water.

Synthesis of FeNC-CVD-gCN catalyst. The mixture of NH_4Cl (Alfa Aesar) and Fe_2O_3 (Sigma Aldrich) with a mass ratio of 2-to-1 was ball-milled for 5 mins. 120 mg of the mixture was placed in a ceramic boat, located upstream of the Ar flow in a quartz furnace tube. 80 mg of Zn-N-C was uniformly dispersed in a thin layer (8 cm × 4 cm) and positioned downstream with an interval distance of two centimeters away from the mixture of NH_4Cl and Fe_2O_3. The furnace continuously flowed argon with a flow rate of 0.65 $L \cdot min^{-1}$ in the pyrolysis process. The furnace was successively held at 40 ℃ and 100 ℃ for one hour, respectively, to remove water and impurities. Following this the furnace temperature was increased to 750 ℃ with a ramping rate of 25 ℃ min^{-1}, and held at 750 ℃ for 3 hours, followed by cooling down to room temperature. The downstream powders were collected and subjected to magnetic purification by slowly moving a small magnet ~ 0.5 cm above the powder layer to remove Fe nanoparticles. The catalyst was labeled as FeNC-CVD-gCN and stored in a vacuum desiccator before electrochemical testing and physicochemical characterization.

Rotating disk electrode (RDE). A thin-film rotating disk electrode was used to evaluate the ORR activities of the Zn-N-C substrate and FeNC-CVD-gCN catalyst. Catalyst inks were prepared by dispersing 10 mg of the catalyst powders in a mixture of Millipore water (36.5 μL, 18.2 MΩ cm) and ethanol (300 μL, Sigma-Aldrich, 99.8%). 5 wt% Nafion solution (108.5 μL, Sigma-Aldrich) was then added into the solution as a binder phase. The resulting mixture was sonicated for 45 minutes in an ice bath, and then an aliquot of 8.8 μL was drop-cast onto a glassy carbon electrode (0.2463 cm^2, Pine instrument) reaching 800 $\mu g \cdot cm^{-2}$ of catalyst loading. The glassy carbon electrode with the deposited catalyst layer as a working electrode was used in a three-electrode cell set-up connected to a potentiostat (Autolab PGstat 30) and rotator (Pine Instruments). A graphite rod and reversible hydrogen electrode (RHE) were used as counter and reference electrodes, respectively. The ORR activities were measured *via* steady-state RDE polarization curves in O_2-saturated 0.5 M H_2SO_4 (95-97%, Sigma-Aldrich) solutions using a rotation rate of 900 *rpm*, 20-mV potential steps from 0.05 to 0.95 V, and a 25-second potential hold time at each step at room temperature. The cyclic voltammetry (*CV*) was carried out between 0.05 to 0.95 V *vs.* RHE with a scan rate of 10 $mV \cdot s^{-1}$ in an Ar-saturated 0.5 M H_2SO_4 solution.

Nitrite stripping. A three-electrode cell was used to conduct nitrite stripping. The working electrode was a 0.2463 cm^2 glassy carbon electrode with 0.27 $mg \cdot cm^{-2}$ catalyst. The counter and reference electrodes were a graphite rod and Ag/AgCl electrode, respectively. A Pt wire was used to correct Ag/AgCl scale to the reversible hydrogen electrode (RHE) scale. A 0.5 M acetate buffer (pH 5.2) was prepared with sodium acetate (Sigma-Aldrich) and glacial acetic acid (Sigma-Aldrich). The experimental procedures included protocols for cleaning, poisoning, and recovery of the working electrode, following the previous report by Malko *et al.*.[36, 38] In brief, the working electrode was subjected to potential cycling from 1.05 V to -0.4 V with scan rates of 100 mV/s and 10 mV/s in Ar-saturated electrolyte (20 cycles). It was repeated until stable *CV*s were obtained. The ORR polarization curves (noted as Unpoisoned) (from 1.0 V to 0.3 V_{RHE}) were collected in O_2-saturated electrolyte using a rotation rate of 900 rpm and a scan rate of 10 $mV \cdot s^{-1}$ followed by the acquisition of a *CV* in Ar-saturated electrolyte in the same potential range. The latter was used to

correct the ORR polarization curves from the point of view of the double-layer capacitance. In addition, the CV curves in the range of 0.4 V to -0.3 V were collected with a scan rate of 10 mV/s. For nitride deposition and subsequent stripping, the working electrode was immersed in 0.125 M $NaNO_2$ solution under rotation at 300 rpm for 5 minutes at open circuit potential (OCP). Subsequently, the working electrode was washed with DI water (1 minute), and electrolyte (5 minutes) with a final rinse in DI water (1 minute) under rotation at 300 rpm. The ORR polarization curves and *CV* curves of the poisoned electrode (noted as Poisoned) as well as its stripping curves were recorded in sequence with the same parameters used for collecting unpoisoned ORR polarization curves. This step was repeated to verify the recovery of ORR polarization curves and features of *CV* curves (noted as Recovered).

Polymer electrolyte membrane fuel cell tests.

MEA_blade_Nafion and MEA_blade_Aquivion: The FeNC-CVD-gCN catalyst/ionomer slurry was prepared with a solvent-to-ionomer mass ratio of 60. The solvent mixture was prepared with a 1:4 ratio (by mass) of isopropanol and deionized water (18.2 mΩ·cm). After the solvent was added to the catalyst, the mixture was sonicated for 10 min. Then, the required amount of ionomer (Nafion D521 or Aquivion D72-25BS (equivalent weight 720 g/mol) solution was added to the mixture. The ionomer-to-carbon ratio was 1. The mixture was sonicated for 2 hours in a bath sonicator, and the temperature of the bath was maintained below 30°C. The slurry was blading coated on the Nafion NR211 membrane. 20 wt% Pt/C (TEC10V20E) was used in the anode electrode with an ionomer-to-carbon ratio of 0.5 (20 wt% Nafion solution (D2020)). The EIS measurements were measured at 0.5 A/cm^2 with the same parameters as for polarization curves in H_2/air conditions.

A commercially available fuel cell hardware (Fuel Cell Technologies, Albuquerque, NM, USA) with a custom flowfield was used for each test. Fabricated MEAs were assembled with a 2.5 cm^2 active area using SGL 29BC gas diffusion layers on both the anode and cathode. Fuel cells were tested using a commercial test station (850e, Scribner Associates Inc., Southern Pines, NC). First, the cell was heated to 80°C with 0.5

L/min of N_2 at 100% RH flowing over the anode and cathode for 2 h to hydrate the membrane and ionomer. Polarization curves were measured under differential conditions with 0.5 L/min of H_2 and 2.0 L/min of air on the anode and cathode respectively. Pressure at the anode and cathode was 150 kpa absolute.

MEA_spray_Nafion: The slurry of FeNC-CVD-gCN catalyst was dispersed into the mixture of water and 1-propanol aqueous (the volume ratio of water to 1-propanol is 4.5). Nafion D521 dispersion (Ion power, 5.0 wt %) was added with the ionomer-to-carbon ratio of 1. The ink was sonicated for an hour and a half in an ice bath before spray-coating on the H23C6 gas diffusion layer (Freudenberg). A thin Nafion overspray layer with a loading of 0.5 mg cm^{-2} was applied to the surface of the cathode electrode to reduce the contact resistance. The anode Pt electrode (47.7 wt% Pt/C (TKK) was fabricated by spray coating ink on the SGL 29-BC gas diffusion layer (Sigracet) with an ionomer-to-carbon ratio of 0.85 and a loading of 0.2 mg cm^{-2}. For membrane electrode assembly (MEA), the anode electrode was first hot-pressed onto NR211 membrane (Ion Power) at 145 °C for 4 minutes, and subsequently, the cathode was hot-pressed onto another side of the Nafion film at 145 °C for 3 minutes. The MEA was integrated into a single cell with single-serpentine flow channels at a compression ratio of around 75%. The single cell was then connected to a fuel cell test station (100 W, Scribner 850e, Scribner Associates). The cells were conditioned under an N_2 environment at 80 °C with 100% relative humidity for 2 hours. Air flowing at 1000 $ml \cdot min^{-1}$ and H_2 (purity 99.999%) flowing at 500 $ml \cdot min^{-1}$ were used for the cathode and anode electrodes, respectively. The total absolute pressure applied to the MEA was 1.5 bar. Fuel cell polarization curves were recorded in a voltage control mode.

Physical characterization

TEM. Transmission electron microscope (TEM) imaging of the ZIF-8/g-C_3N_4 precursor was conducted on a JEOL 2010 field emission gun (FEG).

STEM-EDS. EDS elemental maps were recorded at STEM mode with Thermo-Fisher Talos F200X at an accelerating voltage of 200 kV. Fe L and N K elemental maps were extracted, and overlaying maps were

generated. High-angle annular dark-field (HAADF) STEM images were collected using a Hitachi HD2700C with the Cs probe corrector operated at 200 kV.

SEM. Scanning electron microscopy (SEM) micrographs of the FeNC-CVD-gCN catalyst and Zn-N-C substrate were obtained with a Hitachi S-4800 apparatus (Hitachi, Tokyo, Japan).

XRD. X-ray diffraction (XRD) patterns were collected by using a PANanalytical X'Pert Pro powder X-ray diffractometer with Cu K_α radiation.

N_2 adsorption/desorption analysis. N_2 sorption analysis was conducted at liquid nitrogen temperature (77K) with a Micromeritics ASAP2020 instrument. Before the measurements, the FeNC-CVD-gCN catalyst and Zn-N-C substrates power were degassed at 200 °C for 2 hours in flowing nitrogen to remove moisture. The micropore size distribution was calculated by the density functional theory (DFT) model and meso- and macropore size distribution was calculated by the Barrett-Joyner-Halenda (BJH) method.

XAS measurements. The *ex situ* XAS spectra at the Zn K-edge for the Zn-N-C substrate and Fe K-edge for the FeNC-CVD-gCN catalysts were collected in transmission mode at the beamline 7-BM of National Synchrotron Light Source II (NSLS-II) of Brookhaven National Laboratory. The XAS data were processed and fitted using the Ifeffit−based Athena and Artemis programs.[39] Scans were calibrated, aligned, and normalized with the background removed using the IFEFFIT suite.[40] The χ(R) were modeled using single scattering paths calculated by FEFF6.[41]

ACKNOWLEDGEMENTS

The US Department of Energy supported this work under award numbers DE-EE0008416 and the Northeastern University Dissertation Completion Fellowship. The ex-situ XAS experiments were performed at the beamlines 7-BM of the National Synchrotron Light Source II, a US Department of Energy (DOE) Office of Science User Facility operated for the DOE Office of Science by Brookhaven National

Laboratory. This research used the Center for Functional Nanomaterials, a US DOE Office of Science Facility, at Brookhaven National Laboratory. G.L. acknowledges the support of the US National Science Foundation through Award 2102655 (N_2 adsorption/desorption analysis). T.A.A., S.K.B. and J.S.S. gratefully acknowledge support from the Laboratory Directed Research and Development program at Los Alamos National Laboratory through project 20200200DR.

CONFLICT OF INTEREST

The authors declare no conflict of interest.

REFERENCES

1. Debe, M. K., *Nature* **2012,** 486 (7401), 43-51.
2. Zitolo, A.; Goellner, V.; Armel, V.; Sougrati, M. T.; Mineva, T.; Stievano, L.; Fonda, E.; Jaouen, F., *Nat Mater* **2015,** 14 (9), 937-42.
3. Jia, Q.; Ramaswamy, N.; Hafiz, H.; Tylus, U.; Strickland, K.; Wu, G.; Barbiellini, B.; Bansil, A.; Holby, E. F.; Zelenay, P.; Mukerjee, S., *ACS Nano* **2015,** 9 (12), 12496-505.
4. Li, J.; Jiao, L.; Wegener, E.; Richard, L. L.; Liu, E.; Zitolo, A.; Sougrati, M. T.; Mukerjee, S.; Zhao, Z.; Huang, Y.; Yang, F.; Zhong, S.; Xu, H.; Kropf, A. J.; Jaouen, F.; Myers, D. J.; Jia, Q., *J Am Chem Soc* **2020,** 142 (3), 1417-1423.
5. Mehmood, A.; Gong, M.; Jaouen, F.; Roy, A.; Zitolo, A.; Khan, A.; Sougrati, M.-T.; Primbs, M.; Bonastre, A. M.; Fongalland, D.; Drazic, G.; Strasser, P.; Kucernak, A., *Nature Catalysis* **2022,** 5 (4), 311-323.
6. Jiao, L.; Li, J.; Richard, L. L.; Sun, Q.; Stracensky, T.; Liu, E.; Sougrati, M. T.; Zhao, Z.; Yang, F.; Zhong, S.; Xu, H.; Mukerjee, S.; Huang, Y.; Cullen, D. A.; Park, J. H.; Ferrandon, M.; Myers, D. J.; Jaouen, F.; Jia, Q., *Nat Mater* **2021,** 20 (10), 1385-1391.
7. Hoon T. Chung; David A. Cullen; Drew Higgins; Brian T. Sneed; Edward F. Holby; Karren L. More; Zelenay, P., *Science* **2017,** 357, 479-484.
8. Asad Mehmood; Mengjun Gong; Frédéric Jaouen; Aaron Roy; Andrea Zitolo; Anastassiya Khan; Moulay-Tahar Sougrati; Mathias Primbs; Alex Martinez Bonastre; Dash Fongalland; Goran Drazic; Peter Strasser; Kucernak, A., *Nature Catalysis* **2022,** 5, 311-323.
9. Michel Lefèvre; Eric Proietti; Frédéric Jaouen; Dodelet, J.-P., *Science* **2009,** 324, 71-74.
10. Osmieri, L.; Wang, H.; Neyerlin, K. C., *Journal of The Electrochemical Society* **2021,** 168 (1).
11. Qiao, M.; Wang, Y.; Wang, Q.; Hu, G.; Mamat, X.; Zhang, S.; Wang, S., *Angew Chem Int Ed Engl* **2020,** 59 (7), 2688-2694.
12. Zhang, H.; Xia, W.; Ge, J.; Tang, J., *Chemical Engineering Journal* **2022,** 429.
13. Pampel, J.; Fellinger, T.-P., *Advanced Energy Materials* **2016,** 6 (8).
14. Han, J.; Bao, H.; Wang, J.-Q.; Zheng, L.; Sun, S.; Wang, Z. L.; Sun, C., *Applied Catalysis B: Environmental* **2021,** 280.
15. Yang, X.; Wang, Y.; Zhang, G.; Du, L.; Yang, L.; Markiewicz, M.; Choi, J.-y.; Chenitz, R.; Sun, S., *Applied Catalysis B: Environmental* **2020,** 264.
16. Xin Wan; Xiaofang Liu; Yongcheng Li; Ronghai Yu; Lirong Zheng; Wensheng Yan, H. W.; Ming Xu4; Shui, J., *Nature Catalysis* **2019,** 2, 259-268.
17. Chen, G.; Liu, P.; Liao, Z.; Sun, F.; He, Y.; Zhong, H.; Zhang, T.; Zschech, E.; Chen, M.; Wu, G.; Zhang, J.; Feng, X., *Adv. Mater.* **2020,** 32 (8), e1907399.
18. Zhu, C.; Shi, Q.; Xu, B. Z.; Fu, S.; Wan, G.; Yang, C.; Yao, S.; Song, J.; Zhou, H.; Du, D.; Beckman, S. P.; Su, D.; Lin, Y., *Adv. Energy Mater.* **2018,** 8 (29).

19. Hoon T. Chung; David A. Cullen; Drew Higgins; Brian T. Sneed; Edward F. Holby; Karren L. More; Zelenay, P., *Science* **2017,** 357, 479–484.
20. Jia, Q.; Ramaswamy, N.; Tylus, U.; Strickland, K.; Li, J.; Serov, A.; Artyushkova, K.; Atanassov, P.; Anibal, J.; Gumeci, C.; Barton, S. C.; Sougrati, M.-T.; Jaouen, F.; Halevi, B.; Mukerjee, S., *Nano Energy* **2016,** 29, 65-82.
21. Jiao, L.; Li, J.; Richard, L. L.; Sun, Q.; Stracensky, T.; Liu, E.; Sougrati, M. T.; Zhao, Z.; Yang, F.; Zhong, S.; Xu, H.; Mukerjee, S.; Huang, Y.; Cullen, D. A.; Park, J. H.; Ferrandon, M.; Myers, D. J.; Jaouen, F.; Jia, Q., *Nat. Mater.* **2021,** 20 (10), 1385-1391.
22. Schneider, P., *Applied Catalysis A: General* **1995,** 129, 157-165.
23. Sebastian storch; helmut bretinger; Maier, W. F., *Applied Catalysis A: General* **1998,** 174, 137-146.
24. Deng, Y.; Chi, B.; Tian, X.; Cui, Z.; Liu, E.; Jia, Q.; Fan, W.; Wang, G.; Dang, D.; Li, M.; Zang, K.; Luo, J.; Hu, Y.; Liao, S.; Sun, X.; Mukerjee, S., *J. Mater. Chem. A* **2019,** 7 (9), 5020-5030.
25. Osmieri, L.; Park, J.; Cullen, D. A.; Zelenay, P.; Myers, D. J.; Neyerlin, K. C., *Current Opinion in Electrochemistry* **2021,** 25.
26. Primbs, M.; Sun, Y.; Roy, A.; Malko, D.; Mehmood, A.; Sougrati, M.-T.; Blanchard, P.-Y.; Granozzi, G.; Kosmala, T.; Daniel, G.; Atanassov, P.; Sharman, J.; Durante, C.; Kucernak, A.; Jones, D.; Jaouen, F.; Strasser, P., *Energy & Environmental Science* **2020,** 13 (8), 2480-2500.
27. Wang, G.; Osmieri, L.; Star, A. G.; Pfeilsticker, J.; Neyerlin, K. C., *Journal of The Electrochemical Society* **2020,** 167 (4).
28. K. C. Neyerlin; Hubert A. Gasteiger; Cortney K. Mittelsteadt; Jacob Jorne; Gu, W., *J. Electrochem. Soc.* **2005,** 152 (6), A1073-A1080.
29. Yuxiu Liu; Michael W. Murphy; Daniel R. Baker; Wenbin Gu; Chunxin Ji; Jacob Jorne; Gasteiger, H. A., *Journal of The Electrochemical Society* **2009,** 156 (8), B970-B980.
30. ChungHyuk Lee; Wilton J. M. Kort-Kamp; Haoran Yu; David A. Cullen; Brian M. Patterson; Tanvir Alam Arman; Siddharth Komini Babu; Rangachary Mukundan; Rod L. Borup; Spendelow, J. S., *Nature Energy* **2023,** 8, 685-694.
31. Gerling, C.; Hanauer, M.; Berner, U.; Andreas Friedrich, K., *Journal of The Electrochemical Society* **2022,** 169 (1).
32. Cruz-Manzo, S.; Greenwood, P., *Journal of Electroanalytical Chemistry* **2021,** 892.
33. D. Malevich; E. Halliop; B. A. Peppley; J. G. Pharoah; Karana, K., *ECS Transactions* **2008,** 16 (2).
34. Zhang, J.; Tang, Y.; Song, C.; Cheng, X.; Zhang, J.; Wang, H., *Electrochimica Acta* **2007,** 52 (15), 5095-5101.
35. Malko, D.; Kucernak, A.; Lopes, T., *Nat. Commun.* **2016,** 7, 13285.
36. Malko, D.; Kucernak, A.; Lopes, T., *J Am Chem Soc* **2016,** 138 (49), 16056-16068.
37. Kim, D. H.; Ringe, S.; Kim, H.; Kim, S.; Kim, B.; Bae, G.; Oh, H. S.; Jaouen, F.; Kim, W.; Kim, H.; Choi, C. H., *Nat Commun* **2021,** 12 (1), 1856.
38. Malko, D.; Kucernak, A.; Lopes, T., *Nat. Commun.* **2016,** 7 (1), 13285.
39. Ravel, B.; Newville, M., *J Synchrotron Radiat* **2005,** 12 (Pt 4), 537-41.
40. Newville, M., *J. Synchrotron Rad.* **2001,** 8, 322-324.
41. A. L. Ankudinov; B. Ravel; J. J. Rehr; Conradson, S. D., *Physical Review B* **1998,** 58 (12), 7565-7576.

Supporting information

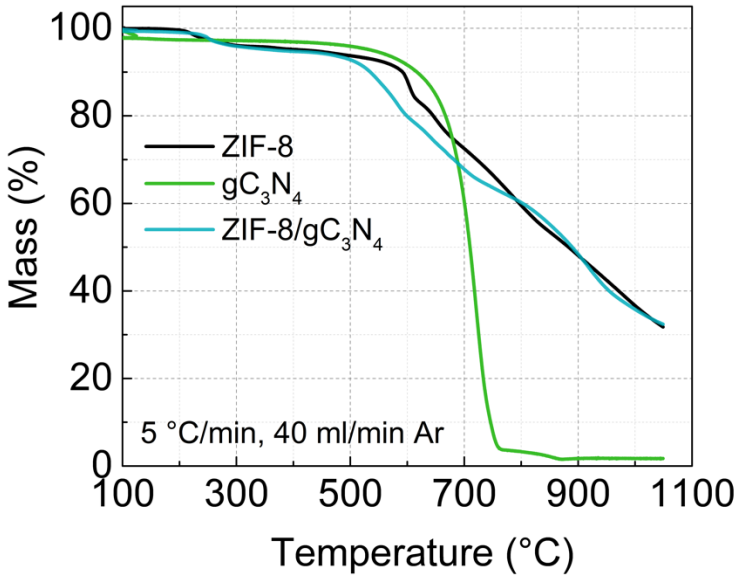

Fig. S1 TGA patterns for ZIF-8 nanoparticles, g-C_3N_4, and integrated ZIF-8/g-C_3N_4 precursor in flowing Ar.

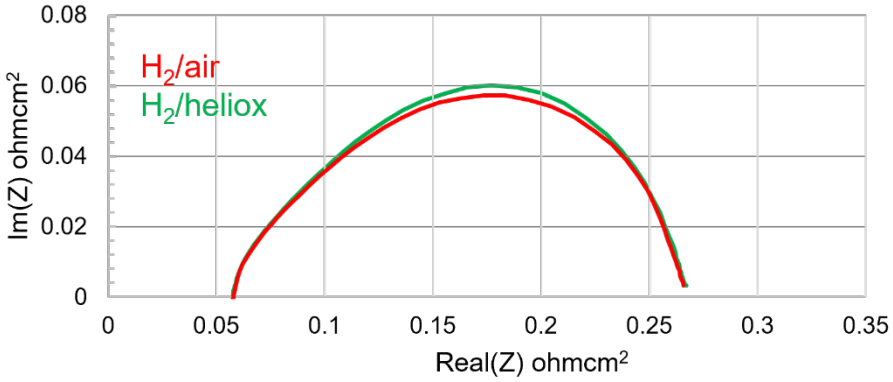

Fig.S2 EIS measurements for H_2/air and H_2/heliox (80 °C, 100 % RH at 0.5 A/cm^2)